Materials
Advances

This article can be cited before page numbers have been issued, to do this please use: I. Ohira, Y. Kono, S. Gréaux, S. Inoué, N. M. Kondo, S. Kakizawa, Y. Higo, N. Tsujino, R. Hrubiak, G. Shen and A. Masuno, *Mater. Adv.*, 2026, DOI: 10.1039/D6MA00275G.

Materials Advances

Volume 01
Number 1
February 2020
Pages 001-200

rsc.li/materials-advances

ISSN 2633-5409

ROYAL SOCIETY OF CHEMISTRY

ROYAL SOCIETY
OF **CHEMISTRY**

rsc.li/materials-advances

View Article Online
DOI: 10.1039/D6MA00275G

Paper

Influence of pressure-induced structural change in Al_2O_3–SiO_2 glasses on the sound velocity and Poisson's ratio under pressure

Submitted 27th February 2026
Received 00th January 20xx,
Accepted 00th January 20xx

DOI: 10.1039/x0xx00000x

Itaru Ohira,*[a] Yoshio Kono,[b] Steeve Gréaux,[c] Sayako Inoué,[c] Nozomi M. Kondo,[d] Sho Kakizawa,[e] Yuji Higo,[e] Noriyoshi Tsujino,[e] Rostislav Hrubiak,[f] Guoyin Shen[f] and Atsunobu Masuno[g]

In this study, we investigated pressure-induced changes in the structure and elastic property of $x$$Al_2O_3$–(100−$x$)$SiO_2$ glasses (x=29, 36, 43, 50, 60 mol.%; referred to as xAS) by *in situ* high-pressure pair distribution function measurement and sound velocity measurement. The 29AS and 60AS glasses are regarded as the Si-rich/Al-rich end-member compositions, and the 36AS, 43AS, and 50AS glasses consist of the two end-member phases in nano-scale. The 29AS glass shows gradual changes in the intermediate-range order up to 9.3 GPa, similarly to SiO_2 glass, while the 60AS glass exhibits a rapid structural change at 7.4–8.4 GPa, similarly to $CaAl_2O_4$ glass. This rapid structural change causes a kink in sound velocity–pressure trend near 8 GPa, as also observed $CaAl_2O_4$ glass. In contrast, the Si-rich end-member 29AS glass does not exhibit the velocity kink.The Poisson's ratios of the five AS glasses and the SiO_2 glass start to converge above ~11 GPa, finally reaching a constant value of ~0.32 at the pressure condition of ~20 GPa. This result indicates that both of the Si-rich and Al-rich end-members have a similar structure above ~20 GPa.

1. Introduction

Densely packed oxide (DPO) glasses synthesized by novel technique such as a container-less levitation method have been attracting attention due to their enhanced functional properties including high elastic modulus and hardness,[1,2] high crack resistance,[3] and high refractive index.[4,5] Such non-conventional glasses consist of various coordinated polyhedra (four-, five-, and six-fold units) that connect with various forms (corner-, edge-, and face-sharing), which yields high packing density.[6] This structural view differs from that of conventional oxide glass, which has a three-dimensional random network of TO_4 tetrahedra (T: network former cation) connected by corner-sharing.

Al_2O_3–SiO_2 (AS) is one of the known systems in which DPO glasses can form. AS glass is not only an advanced functional glass having high hardness and toughness,[3] but it is also important in geoscience as an analogue for extracting the difference in the structural roles of Si and Al in magmas under pressure.[7,8] To discuss the relationship between structure and composition in this binary system, it is necessary to understand the structural differences between single component glasses: SiO_2 and Al_2O_3 glasses. SiO_2 glass is the representative network glass, which has a three-dimensional Si–O network formed by the connection of corner-sharing SiO_4. Because no network modifier cation exits in its structure, SiO_2 glass has a large cavity volume of ~30%,[9] which leads to low packing density. On the other hand, Al^{3+} does not behave as a network former alone, and therefore Al_2O_3 melt cannot be vitrified by conventional melt–quenching technique. Some recent techniques such as sol-gel method, thin-film fabrication, and anodization for metal Al enable the vitrification of Al_2O_3. The Al_2O_3 glass prepared by the anodization contains ~60% of Al ions in five- or six-coordination, and ~19% of the Al–O polyhedra form edge-sharing connectivity in its structure.[10,11] Coexistence of the various structural units enables Al_2O_3 glass to achieve high packing density.

Binary AS glass is known to have a wide immiscible gap, where the glasses are composed by nanoscale Si-rich and Al-rich domains.[12–16] For investigation of the local structure in each domain, Liao et al. (2020) analysed 50 mol.% Al_2O_3–50 mol% SiO_2 glass using electron energy loss fine structure in the scanning transmission electron microscope.[14] Their analyses demonstrated that the Si-rich domain has a structure similar to that of SiO_2 glass, with corner-sharing $(Si,Al)O_4$ units that form a glass network. On the other hand, ~60% of the Al ions in the Al-rich domain exist in the form of high-coordination (i.e., AlO_5 and AlO_6), behaving as network modifiers, which is similar to Al_2O_3 glass. Although the range of immiscibility in this system has not been well constrained, the Al-rich end-member probably has a mullite-like composition (approximately 60 mol.% Al_2O_3–40 mol% SiO_2, 60AS).[15,16] In addition, a NMR study on the 60AS

---

[a] Department of Chemistry, Gakushuin University, Tokyo 171-8588, Japan. Email: itaru.ohira@gakushuin.ac.jp
[b] Department of Physics and Astronomy, Kwansei Gakuin University, Sanda 669-1330, Japan.
[c] Geodynamics Research Center, PIAS, Ehime University, Matsuyama 790-0826, Japan.
[d] Institute for Planetary Materials, Okayama University, Misasa, Tottori 682-0193, Japan.
[e] Japan Synchrotron Radiation Research Institute, Sayo-gun, Hyogo 679-5198, Japan.
[f] High Pressure Collaborative Access Team, X-ray Science Division, Argonne National Laboratory, Argonne, Illinois 60439, USA.
[g] Graduate School of Engineering, Kyoto University, Kyoto 615–8520, Japan.

glass showed that it contains Al in 4-, 5-, and 6-fold coordination in the approximate ratio 4:5:1.[17] The presence of high-coordinated Al is consistent with the pioneering results of XRD, Raman, NMR measurements on 60AS glass synthesized by other novel techniques.[18–22] Therefore, the Al-rich domain formed in the immiscible region is considered to be a densely packed structure similar to Al_2O_3 glass.

In addition to the compositional effect, pressure is another important factor to form densified glasses. Under room temperature compression, SiO_2 glass exhibits an almost linear increase in density up to at least 20 GPa.[23–25] The density change may result from multiple densification processes. It has been reported that SiO_2 glass undergoes collapse of the silicon's second shell into the first shell, which breaks local tetrahedral symmetry, at the pressure region above 2.3 GPa.[26] After completion of this breaking of local tetrahedral symmetry, its nearest-neighbour Si–O coordination number (CN) from 4 to 6 at ~10–40 GPa.[27–32] These two different structural changes result in distinct behaviours of sound velocity. The breaking of local tetrahedral symmetry yields an anomalous elasticity minimum under compression around that pressure region,[33–36] while the Si–O CN increase above 10 GPa causes a gradual increase in longitudinal wave velocity (v_L) and the transverse wave velocity (v_T).[34–36] Such pressure-induced densification is considered to be also occurred in DPO glass. However, the structural changes may differ from that of the network glass with large void volume. For example, the study on $CaAl_2O_4$ glass, which is one of the DPO glasses, showed a pressure-induced polyamorphic transition accompanied by discontinuous increase in v_L and v_T over the narrow pressure range of 8–10 GPa, which is driven by the disappearance of the large void between Ca and O atoms.[36] Similarly to the $CaAl_2O_4$ glass, the high-coordinated Al ions in the Al-rich end-member in the AS glass may play a role similar to that of the Ca ions in that aluminate glass.

In this study, we have investigated the pressure-induced changes in structure and elastic properties of $x$$Al_2O_3$–(100−$x$)$SiO_2$ glasses (x=29, 36, 43, 50, 60 mol.%; referred to as xAS). The AS glasses were prepared across the immiscible region of Al_2O_3–SiO_2 system. The 29AS and 60AS homogeneous glasses are defined as the Si-rich and Al-rich end-members, respectively, while the 36AS, 43AS, and 50AS glasses exhibit nano-scale phase separation, composed of the two end-members. To understand the high-pressure structural changes in the Si-rich and Al-rich end-members, the structure factor $S(Q)$ and the pair-distribution function $g(r)$ were determined for the 29AS and 60AS glasses. In addition, the sound velocity and Poisson's ratio of the five AS glasses were determined under pressure. Based on the structural data and velocity–pressure trends of the AS glasses, we conclude that the Al-rich end-member undergoes a rapid structural change characterized by a velocity kink near 8 GPa, followed by structural convergence with the Si-rich end-member above ~20 GPa.

2. Experimental methods

2. 1. Sample synthesis and chemical analysis

Five $x$$Al_2O_3$–(100−$x$)$SiO_2$ glasses (x=29, 36, 43, 50, and 60, referred to as 29AS, 36AS, 43AS, 50AS, and 60AS) were synthesized by using container-less laser-heating levitation method. We used the 50AS and 60AS glasses reported in ref. 3. In addition, we synthesized three samples (29AS, 36AS, and 43AS glasses) using an aerodynamic levitator with a 200 W CO_2 laser at GRC, Ehime University. For the synthesis of the three glasses, SiO_2 (quartz, 99.9%, c.a. 4 μm, Kojundo Chemical Laboratory) and Al_2O_3 (>99%, Wako) powders were heated at 1473 K for 2 h in air by an electric furnace to remove water. The dried powders were weighed with the stoichiometric ratios of $x$$Al_2O_3$–(100−$x$)$SiO_2$ (x=20, 30, 40) and were mixed in ethanol using an agate mortar for 1 h. The powder mixtures were compressed to cylindrical shape by a pellet die (2 mm in diameter), which were melted in the aerodynamic levitation furnace by laser heating. After confirmation of total melting by a high-speed camera, we turned off the laser for quenching the spherical melt sample to form glass. Because of evaporation of SiO_2 during melt processing, the Al_2O_3 contents in the synthesized glasses are higher than those in the starting powders.[12] Indeed, the compositions of the 29AS (Al_2O_3 = 28.59±0.14 in mol.%, n = 20), 36AS (36.11±0.07, n = 20), and 43AS (42.92±0.07, n = 30) glasses were synthesized from the starting powder compositions with x = 20, 30, 40, which were examined by scanning electron microscopy (JEOL JMS-6360) with energy-dispersive spectroscopy (Oxford INCA energy 300) at Gakushuin University.

The analyses of the AS glass samples recovered after the high-pressure ultrasonic measurements were performed using a JEOL JEM 2100F field emission scanning trans-mission electron microscope operating (STEM) system equipped with a JEOL JED-2300T Energy Dispersive X-ray spectrometer (EDS). The EDS spectra data were obtained and processed by using ThermoFischer Scientific Noran System 7. Thin foil of about 100 nm thick was prepared by focused ion beam (FIB) lift-out technique using, Thermo Fisher Scientific Scios and Scios2 dual-beam FIB-SEM system.

2. 2. *In situ* high-pressure pair distribution function measurements

The Structure factors, $S(Q)$, of the 60AS glass under pressure were obtained by *in situ* multiangle energy-dispersive x-ray diffraction (EDXD) measurements in a Paris-Edinburgh press at the beamline 16-BM-B of the APS. Details of the high-pressure experimental setup at beamline 16-BM-B and the analytical procedures have been previously reported.[36,37] We used a cupped-Drickamer-toroidal (CDT) cell, same as the previous study on $CaAl_2O_4$ glass.[36] A piece of gold was placed at the edge of the glass sample to avoid contamination of its x-ray diffraction peaks into that of the glass sample. The gold was used for determination of experimental pressure by the equation of state of gold.[38] In high-pressure multiangle EDXD measurements, we collected a series of EDXD patterns of the 60AS glass sample at 2θ angles of 3.0, 4.0, 5.0, 7.0, 9.0, 12.0, 15.0, 18.0, 22.0, 26.0, 30.0, and 35.0° at each pressure point. The $S(Q)$ was determined from the collected EDXD patterns using the software packages hpMCA and aEDXD developed in the 16-BM-B beamline.[37,39] The pair distribution function $g(r)$ was calculated by Fourier transform of the $S(Q)$. The sample density (ρ) at high-pressure (P) used in this Fourier transform is estimated from the results of high-pressure sound velocity measurement using the ambient density (ρ_0) through the relationship:

$$\rho = \rho_0 + \int_{P_0}^{P} \frac{\gamma}{\left(v_{\mathrm{L}}^2 - \frac{4}{3} v_{\mathrm{T}}^2\right)} dP, \qquad (1)$$

where P_0 is the initial pressure (10^{-4} GPa), v_{T} and v_{L} are longitudinal and transverse wave velocities, and γ is the ratio of the isothermal and adiabatic bulk moduli that is taken to be 1 for the samples at room temperature.

The $S(Q)$ of the 29AS glass were obtained by *in situ* angle-dispersive x-ray diffraction (ADXD) measurements at the BL15XU beamline in SPring-8. We used a pink-beam at a photon energy of 100.34 keV. Similar to the EDXD measurements, we used CDT cell in the Paris-Edinburgh press for high-pressure experiment, and gold was used as the pressure scale.[38] XRD patterns were collected at the 2θ angles between 0.4 and 16.8°. The details of the experimental setup and analytical process of $S(Q)$ and $g(r)$ were reported elsewhere.[40] The density of the 29AS glass was estimated from its sound velocity data, same as that of the 60AS glass.

2. 3. *In situ* high-pressure sound velocity measurement

The sound velocities of the five AS glasses at high pressures were determined by *in situ* x-ray and ultrasonic measurements in a Kawai-type 1500 ton multi-anvil press (SPEED-1500) at the beamline BL04B1 in SPring-8.[41,42] The cell assembly used in the study is shown in Figure S1. The glass samples were shaped into a cylindrical shape (1.5 or 2.0 mm in diameter and ~1 mm in length) and placed at the centre of a MgO sleeve. Both sides of the samples were polished using a 0.5 μm diamond polishing mat. We placed an Al_2O_3 buffer rod for transmitting elastic waves from the WC anvil to the sample, and a backing material (NaCl with 10 wt.% gold) was placed at the back side of the sample. A gold foil (2 μm thickness) was inserted between each interface (buffer rod/sample and sample/backing material) to enhance mechanical coupling for elastic wave propagation and to mark sample interfaces for sample length measurement.

White X-ray radiography images were obtained using a CMOS camera with a resolution of 1.31 μm/pixel. Sample length was determined from the distance between the two gold foils on the top and bottom faces of the sample at each pressure point.[41,43] For pressure determination, energy-dispersive x-ray diffraction (EDXD) measurements were conducted for the backing material (mixture of NaCl and Au) at a fixed diffraction angle of 5.9980° (29AS), 5.9988° (36AS), 5.9778° (43AS), 6.0071° (50AS), or 6.0069° (60AS). The gold in the backing material is used as pressure scale.[38] Ultrasonic measurements were carried out at each pressure condition using the pulse–echo-overlap method. The acoustic echo measurements were performed at the frequency of 50–70 MHz for longitudinal waves and 30–50 MHz for transverse waves. The two-way travel time was analysed by using an analysis program,[43] and the mean and standard deviation of the travel times obtained from different frequency are defined as the best estimate and error, respectively. The errors of travel time were up to 0.6% (longitudinal wave) and 0.4% (transverse wave), respectively. The errors of sample length analysis were up to ±6.7 pixel (±9 μm, 1.2%). The overall uncertainties of longitudinal and transverse wave velocities (v_{L} and v_{T}, respectively) are up to 1.2%. The numerical data of v_{L} and v_{T} with their uncertainties are shown in Tables S1–S5 in the Supplemental Material.

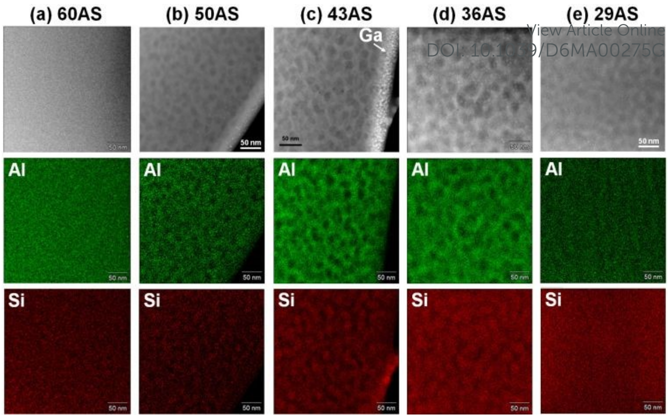

Fig. 1 ADF-STEM images of **(a)** 60AS, **(b)** 50AS, **(c)** 43AS, **(d)** 36AS, and **(e)** 29AS glasses recovered from *in situ* high-pressure x-ray ultrasonic measurements. The top, middle, bottom rows exhibit the ADF-STEM images and the elemental mapping images for Al and Si of each sample, respectively. The white particles on the ADF-STEM images are gallium (Ga) contamination deposition formed during FIB processing.

3. Results and discussion

3. 1. Nano-texture in the AS glasses

Figure 1 exhibits annular dark-field (ADF)-STEM images of the AS glasses recovered after the high-pressure sound velocity measurements. The 60AS glass has a homogenous texture (Fig. 1a), while the 50AS (Fig. 1b), 43AS (Fig. 1c), and 36AS (Fig. 1d) glasses show nano-scale phase separation. The 50AS, 43AS, and 36AS glasses are composed of the nano-scale Si-rich and Al-rich domains (Figs. 1b–d and Table S6). The 50AS glass exhibits binodal decomposition, in which the Si-rich domains of ~10–20 nm in size isolated (Fig. 1b), as observed in the previous STEM analysis.[14] In contrast, the 43AS glass has a morphology of spinodal decomposition, where the nano-scale Si-rich domains were inter-connected similar to the Al-rich matrix (Fig. 1c). Compared to the 43AS glass, the connections between Si-rich domains become more developed in the 36AS glass (Fig. 1d). The transition boundary from the spinodal regime to the binodal regime lies between 50AS and 43AS, which is consistent with the previous thermodynamic analysis.[15] The 29AS glass appears to show the two texture in the ADF-STEM image (Fig. 1e). However, the STEM-EDS analyses show no compositional difference between the dark and bright domains (Table S6). These results indicate that the 36AS, 43AS, and 50AS glasses have the nano-scale phase separation texture,

View Article Online
DOI: 10.1039/D6MA00275G

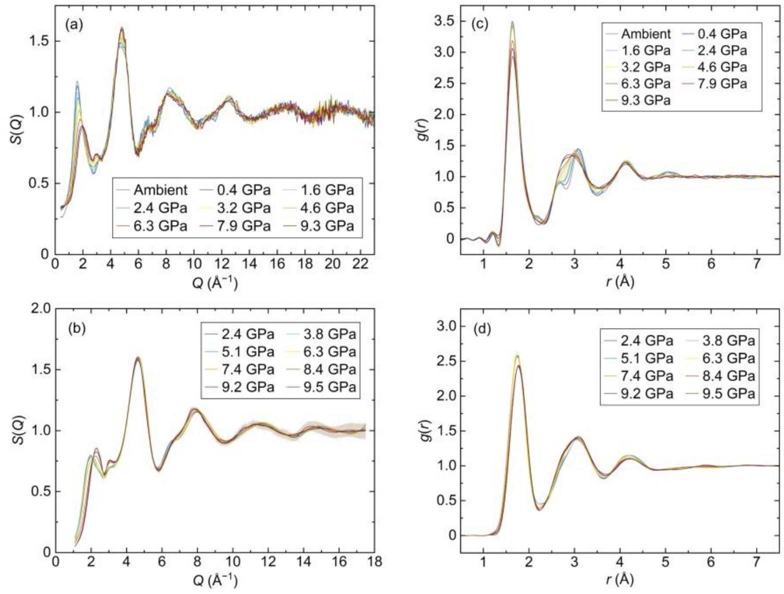

Fig. 2 Total structure factor $S(Q)$ and pair-distribution functions $g(r)$ for the 29AS and 60 AS glasses at high-pressure conditions. **(a)** The $S(Q)$ of the 29 AS glass obtained by the ADXD measurement at the BL15XU, SPring-8. **(b)** The $S(Q)$ of the 60 AS glass obtained by *in situ* multiangle EDXD measurement at the 16-BM-B, APS. **(c)** the $g(r)$ of the 29AS glass determined from $S(Q)$ shown in (a). **(d)** the $g(r)$ of the 60AS glass determined from $S(Q)$ shown in (b). A typical size of the error in the EDXD measurements is indicated by the brown vertical bars for the $S(Q)$ data at 9.5 GPa. The $S(Q)$ and $g(r)$ data with offsets to avoid overlap of each pattern are provided in Figs. S2 and S3 in the supplementary information.

while the 60AS and 29AS glasses can be regarded as homogeneous glasses composed of Al-rich and Si-rich end-members within the investigated composition range, respectively.

3. 2. Structure factor $S(Q)$ and pair-distribution function $g(r)$ of AS glasses under compression.

Figure 2 exhibits experimentally determined $S(Q)$ and $g(r)$ of the 29AS (Si-rich end-member) and 60AS (Al-rich end-member) glasses at high-pressure conditions from 0.4 GPa to 9.5 GPa. In the 29AS glass, the intensity of the first sharp diffraction peak (FSDP) decreases together with the shift of the peak position to high-Q up to 9.3 GPa (Fig. 2a). The behaviour of the FSDP in the 29AS glass is similar to those of SiO_2 glass.[26,28,32] The FSDP in the $S(Q)$ of the 60AS glass also shifts to higher Q, but it does not show a clear intensity reduction up to 7.4 GPa (Fig. 2b). Above 7.4 GPa, however, the intensity turns to increase, which is similar to the observation in $CaAl_2O_4$ glass.[36]

In addition to the changes in the FSDPs, the second peaks at ~3 Å^{-1} grow with increasing pressure. The second peak of the 29AS glass gradually grows over the experimental pressure range (Fig. 2a). The development of the second peaks is likely attributed to breaking of local tetrahedral symmetry and increase in packing density of oxygen atoms, as reported in the pressurised SiO_2 glass.[26,30,44] On the other hand, the second peak of the 60AS exhibits no clear change in its intensity below 7.4 GPa, and it abruptly increases between 7.4–8.4 GPa (Fig. 2b). Unlike SiO_2 glass, the 60AS glass does not have the tetrahedral symmetry due to the presence of the 5- and 6-fold Al ions. The abrupt intensity increase observed in the 60AS glass can be attributed to an increase in topological ordering due to a transition to a more densely packed structure, as observed in $CaAl_2O_4$ glass.[36]

Figures 2c and 2d shows the $g(r)$ of the 29AS and 60AS glasses, derived from the experimentally determined $S(Q)$ (Figs. 2a, b). The first peak ($r1$) in the $g(r)$ is assigned to average T–O bond distance (T = Al, Si). Since the ionic radii of 4-, 5-, and 6-fold Al^{3+} (0.39, 0.48, 0.535 Å) is larger than that of 4-fold Si^{4+} (0.26 Å),[45] the $r1$ shifts to higher r with increasing Al_2O_3 content. The $r1$ of the 29AS glass stays at ~1.64 Å up to 9.4 GPa (Fig. S3). This behaviour is similar to that of SiO_2 glass, where Si–O bond distance and CN start to increase above ~10–15 GPa.[27–29] On the other hand, the $r1$ of the 60AS glass locates at ~1.75 Å below 7.4 GPa, and starts to shift toward high-r side at the high pressures (Fig. S4). The result indicates that the average T–O CN of the 60AS glass starts to increase from ~8 GPa. It has been reported that the T–O CN of the 60AS glass reaches six at ~20 GPa, with a T–O bond length of ~1.81 Å.[8]

The difference in $g(r)$ between the two glasses becomes more obvious in the long correlations. The unpressurised 29AS glass is considered to be dominated by a network formed by corner-sharing TO_4 tetrahedra, resulting in the development of two peaks due to the correlations of O–O at ~2.6 Å (the second peak) and corner-sharing T–T (the third peak) at ~3.0 Å (Fig. 2c), same as SiO_2 glass (e.g., ref. 27). As pressure increases, the second and third peaks gradually converge, eventually merging into a single peak. (Fig. 2c). This is explained by the decrease of T–T distance, likely due to bending of the T–O–T inter-tetrahedral angles upon compression, similarly to the observation in SiO_2 glass,[27,32] which supports the structural analogy between the 29AS and SiO_2 glass. In contrast, the unpressurised 60AS glass contains various correlations due to O–O bond, corner- and edge-sharing T–T, and the second nearest-neighbour T–O at the r range between ~2.6 Å and ~3.4 Å even at ambient pressure.[19,20] This results in the broad peak without clear pressure dependence (Fig. 2d). This static behaviour of the merged peak around 3 Å is similar to that of $CaAl_2O_4$ glass, which is one of the DPO glasses.[36] Interestingly, the 29AS and 60AS glasses show similar $g(r)$ at the highest pressure. This result implies that both the 29AS and 60AS glasses have the similar intermediate-range framework above ~10 GPa.

3. 3. Sound velocity–pressure trends of AS glasses up to 24 GPa and its structural interpretation

Figure 3 exhibits the v_L and v_T of the five AS glasses under compression to 24.3 GPa, determined by *in situ* high-pressure ultrasonic measurements at the BL04B1 beamline, SPring-8. The velocity–pressure trends of SiO_2 glass determined by the previous

View Article Online
DOI: 10.1039/D6MA00275C

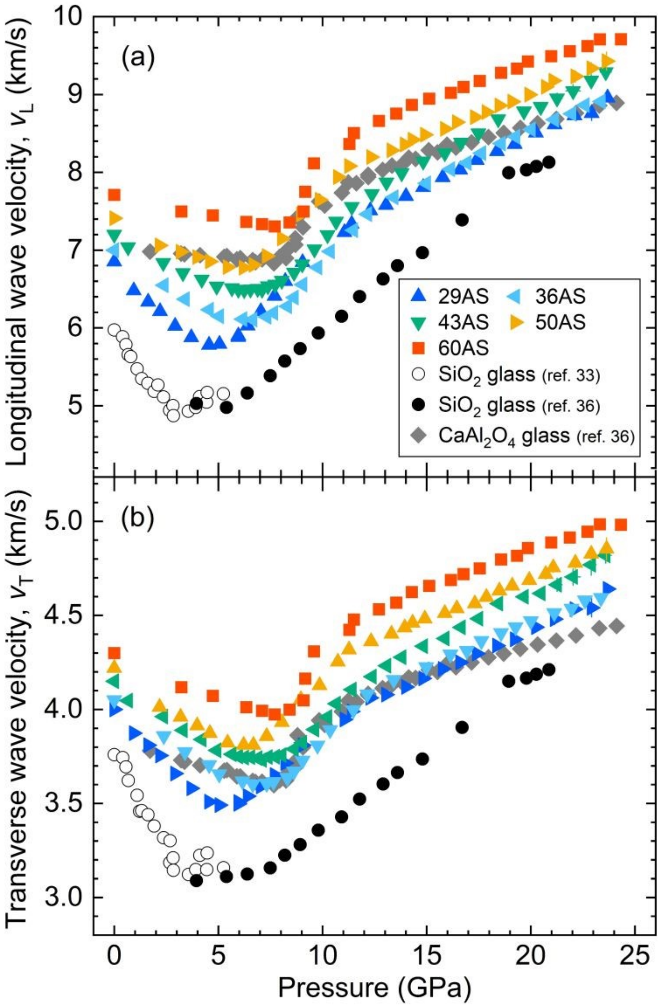

Fig. 3 **(a)** Longitudinal wave velocity (v_L) and **(b)** transverse wave velocity (v_L) of the five AS glasses (this study), SiO_2 glass,[33,36] and $CaAl_2O_4$ glass[36] determined by the ultrasonic method under compression. The sound velocities at atmospheric pressure (10^{-4} GPa) are estimated from the previously measured data.[3] The numerical data of the AS glasses are shown in Tables S1–S5 in the supplementary information.

ultrasonic measurements are also shown.[33,36] SiO_2 glass shows a rapid decrease in v_L and v_T up to ~2–3 GPa, followed by a linear increase up to at least ~20 GPa. The 29AS glass (Si-rich end-member) exhibits behaviour similar to SiO_2 glass in the v_L–P and v_T–P trends, as well as for the changes in $S(Q)$ and $g(r)$ (Fig. 2). However, the pressure condition of the velocity minimum increases to higher pressure of ~5 GPa (5.1 GPa for v_L and 4.6 GPa for v_T) (Fig. 3 and Table S1). In addition, the v_L and v_T values of the 29AS glass are higher than those of SiO_2 glass. This indicates that the 29AS glass is stiffer than SiO_2 glass because the bulk and shear moduli increase with increasing Al_2O_3 content in the binary aluminosilicate glasses.[3]

On the other hand, the v_L–P and v_T–P trends of the 60AS glass (Al-rich end-member) are similar to those of $CaAl_2O_4$ glass up to 24 GPa (Fig. 3). The velocity minima are observed at 7.7 GPa for both v_L and v_T, and then the velocities rapidly increase up to 11.3 GPa, followed by a linear increase at the higher pressure (Fig. 3 and Table S5). As a result, the 60AS glass has a kink in the dv_L/dP and dv_T/dP (hereafter, "velocity kink") in the pressure region of 8–11 GPa. In addition to the velocity kink, this glass also exhibits the rapid reduction of sample length in this pressure region (Fig. S5). These elastic anomalies at that pressure region are also observed in $CaAl_2O_4$ glass.[36] Above ~11 GPa, however, both the two end-member glasses exhibit the linear increase in velocity with almost same slope (29AS: dv_L/dP = 0.1279(13), dv_T/dP = 0.0496(9); 60AS: dv_L/dP = 0.0987(20), dv_T/dP = 0.0416(9); Table S7). The gradual velocity increase in the 29AS and 60AS above ~11 GPa likely reflects the gradual increase in average T–O CN, which is also observed in SiO_2[34–36] and $CaAl_2O_4$[36] glasses.

The onset of the velocity kink for the 60AS glass is observed at the pressure condition where the FSDP and second peak in $S(Q)$ increase in intensity (Fig. 2a) and the $r1$ in $g(r)$ starts to shift to high r (Figs. 2c and S4). Therefore, the 60AS glass, which has a densely packed structure even at ambient conditions, transforms into further densely packed state at ~8 GPa. Interestingly, the NMR spectroscopic studies of Al_2O_3 and $Mg_3Al_2Si_3O_{12}$ glasses cycled to high pressure demonstrated that the irreversible increase of Al–O CN progresses only over ~6–10 GPa, and that the fraction of high-coordinated Al^{3+} ions preserved in the decompressed samples does not change above ~12 GPa.[46,47] Therefore, the structural changes accompanied by the velocity kink around 8 GPa may develop the irreversible densification. Indeed, it has been confirmed that $CaAl_2O_4$ glass recovered from 16 GPa (~6 GPa higher than the end point of velocity kink) undergoes irreversible densification.[36]

The velocity-pressure trends of the 36AS, 43AS, and 50AS glasses, which have the nano-scale phase separation textures, exhibit a velocity kink and reduction of sample length at ~7–11 GPa (Figs. 3 and S5). Based on presence of the elastic anomalies, the pressure-induced structural changes that occurred in the three glasses are similar to the 60AS glass than the 29AS glass. Moreover, the velocity kink becomes unclear with decreasing Al_2O_3 content (increasing of the Si-rich domain) (Fig. 3). Since the three phase-separating glasses contain the Al-rich domain (Figs. 1b–d, Table S6) that can behave similarly to the 60AS glass, their velocity kinks are considered to be caused by the rapid structural change in this domain.

3. 4. Structural convergence of the AS glasses above 20 GPa

Poisson's ratio (σ) is calculated using the measured v_L and v_T by the following equation:

$$\sigma = \frac{{v_L}^2 - 2{v_T}^2}{2({v_L}^2 - {v_T}^2)}. \qquad (2)$$

Poisson's ratio is known to increase with increasing the atomic packing density (C_g), and the C_g correlates with the glass network dimensionality (e.g., ref. 48). For example, SiO_2 and Si-rich silicate glasses that have the three-dimensional random network with a large fraction of free volume exhibit small Poisson's ratios (σ <0.2). On the other hand, the DPO glasses such as Al-rich aluminosilicate and aluminate glasses containing the various structural motifs (network modifier 5- and 6-fold Al^{3+}, edge-sharing AlO_x polyhedra) lose the fully polymerized three-dimensional network even at ambient conditions, which leads to their high Poisson's ratios and C_g.[48] Consequently, in the system Al_2O_3–SiO_2, the Poisson's ratio of

View Article Online
DOI: 10.1039/D6MA00275C

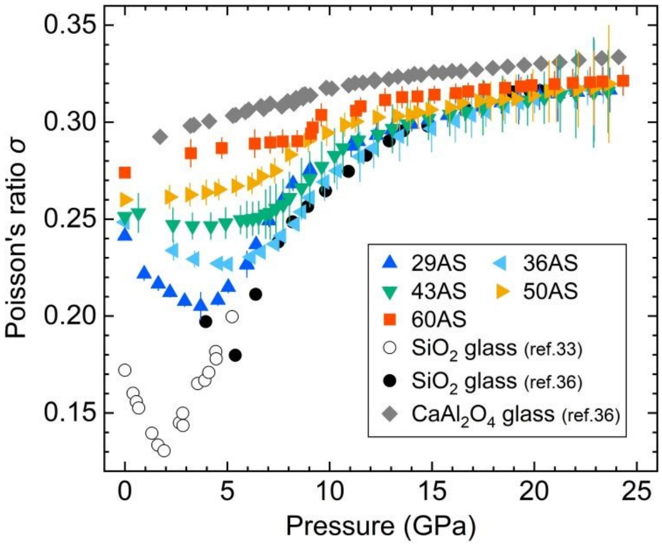

Fig. 4 Poisson's ratio (σ) of the five AS glasses (this study), SiO_2 glass,[33,36] and $CaAl_2O_4$[36] calculated from the sound velocity data. The numerical data of the AS glasses are shown in Tables S1–S5 in the supplementary information.

unpressurised glasses ranges from 0.190 for the SiO_2 glass to 0.274 for the 60AS glass.[3] This reflects the progression of densely packed state due to by addition of Al_2O_3. In the initial stage of pressurisation below ~5 GPa, the Poisson's ratio of the 29AS, 36AS, and 43AS glasses exhibits negative pressure dependence, while those of the 50AS and 60AS glasses exhibit positive pressure dependence (Fig. 4). Above 5 GPa, all of the AS glasses show positive pressure dependence (Fig. 4). At ~5–8 GPa, the increase rate of σ increases with Al_2O_3 content, resulting in the σ of the 29AS glass being larger than those of the 36AS and 43AS glasses.

After the completion of the velocity kink at ~11 GPa, the difference in the σ values among the AS glasses becomes small, which are finally converged to ~0.32 at ~20 GPa (Fig. 4). This result implies that both of the Si-rich and Al-rich end-members of our study have a very similar atomic packing state at that pressure. The converged value of 0.32 is comparable with those of metallic glasses (σ = 0.3–0.4).[49,50] The metallic glasses have zero-dimensional cluster-based network.[48] Therefore, both the Si-rich and Al-rich end-member glasses are considered to have such a weakly correlated network at >20 GPa.

Conclusions

We conducted the *in situ* high-pressure pair-distribution function and sound velocity measurements on the AS glass samples. The 29AS glass, Si-rich end-member glass within the investigated composition range, exhibits the gradual change in the intermediate-range order up to 9.3 GPa, similarly to that observed in SiO_2 glass. In contrast, the 60AS glass, Al-rich end-member glass, shows the changes in both the intermediate- and short-range orders only at 7.4–8.4 GPa. The sound velocity data indicate that the densification process of the AS glasses is divided into three distinct pressure regions: (i) the low pressure region up to the velocity minimum; (ii) the middle pressure region, where v_L and v_T quickly increase (the velocity kink); (iii) the high pressure region with a gentle and linear gradient. In the region (i), the variation in the velocity–pressure trends of the AS glasses likely arise from the difference in the C_g of the initial structures. In the region (ii), the velocity kink becomes distinct with increasing Al_2O_3 content, indicating that the Al-rich end-member undergoes the rapid structural change at ~7–11 GPa, resulting in the velocity kink. In the region (iii), the Poisson' ratios of the five AS glasses and SiO_2 glass converge, and finally become same within the errors. This result indicates that at >20 GPa both of the Si-rich and Al-rich end-member phases are considered to have a weakly correlated network, such as a zero-dimensional cluster-based network observed in metallic glasses.

Author contributions

I. Ohira: Conceptualization, Data curation, Formal analysis, Funding acquisition, Investigation, Methodology, Project administration, Resources, Visualization, Writing – original draft. Y. Kono: Funding acquisition, Investigation, Software, Writing – review and editing. S. Gréaux: Formal analysis, Funding acquisition, Investigation, Methodology, Resources. S. Inoué: Investigation, Visualization, Writing-review and editing. N. M. Kondo: Investigation. S. Kakizawa: Investigation, Resources, Software. Y. Higo: Resources, Software. N. Tsujino: Resources, Software. R. Hrubiak: Resources, Software, Writing – review and editing. G. Shen: Investigation, Resources. A. Masuno: Resources.

Conflicts of interest

There are no conflicts to declare.

Data availability

The data supporting this article have been included as part of the supplementary information (SI). Supplementary information: Schematic diagram of the high-pressure cell for sound velocity measurement, $S(Q)$ and $g(r)$ with vertical offset, pressure dependence of $r1$ and sample length, and numerical values of measured sound velocity and chemical composition. See DOI: [URL – format https://doi.org/DOI].

Acknowledgements

This paper is supported by JSPS KAKENHI (Grants No. JP20K22369, No. JP23K13193, No. JP22K18736, No. JP23KK0065, No. JP19H02002, and No. JP23K25970) and the Joint Usage/Research Center PRIUS, Ehime University, Japan. The experiments were conducted at the beamlines BL04B1 and BL15XU in SPring-8 (JASRI Proposals No. 2020A0069, No. 2020A1712, and No. 2022B1171). A part of this research was performed on APS beam time award (DOI: 10.46936/APS-178398/60015783) from the Advanced Photon Source, a U.S. Department of Energy (DOE) Office of Science user facility operated for the DOE Office of Science by Argonne National Laboratory under Contract No. DE-AC02-06CH11357. HPCAT

DOI: 10.1039/D6MA00275G

operations are supported by DOE-NNSA's Office of Experimental Sciences.

References

1 G. A. Rosales-Sosa, A. Masuno, Y. Higo, H. Inoue, Y. Yanaba, T. Mizoguchi, T. Umada, K. Okamura, K. Kato and Y. Watanabe, *Sci. Rep.*, 2015, **5**, 15233.

2 Y. Guo, J. Li, Y. Zhang, S. Feng and H. Sun, *iScience*, 2021, **24**, 102735.

3 G. A. Rosales-Sosa, A. Masuno, Y. Higo and H. Inoue, *Sci. Rep.*, 2016, **6**, 23620.

4 Y. Arai, K. Itoh, S. Kohara and J. Yu, *J. Appl. Phys.*, 2008, **103**, 094905.

5 A. Masuno and H. Inoue, *Appl. Phys. Express*, 2010, **3**, 102601.

6 A. Masuno, *J. Phys. Soc. Jpn.*, 2022, **91**, 091003.

7 I. Ohira, M. Murakami, S. Kohara, K. Ohara and E. Ohtani, *Prog. Earth Planet. Sci.*, 2016, **3**, 18.

8 I. Ohira, Y. Kono, C. Kenney-Benson, A. Masuno and G. Shen, *Geochem. Persp. Let.*, 2019, **10**, 41–45.

9 S. Kohara, J. Akola, H. Morita, K. Suzuya, J. K. R. Weber, M. C. Wilding and C. J. Benmore, *Proc. Nat. Acad. Sci. U. S. A.*, 2011, **108**, 14780–14785.

10 H. Hashimoto, K. Yazawa, H. Asoh and S. Ono, *J. Phys. Chem. C*, 2017, **121**, 12300–12307.

11 H. Hashimoto, Y. Onodera, S. Tahara, S. Kohara, K. Yazawa, H. Segawa, M. Murakami and K. Ohara, *Sci. Rep.*, 2022, **12**, 516.

12 S. K. Wilke, C. J. Benmore, V. Menon, J. Ilavsky, A. Rezikyan, R. E. Youngman, M. P. Carson and R. Weber, *J. Am. Ceram. Soc.*, 2023, **106**, 2820–2834.

13 S. Sen and R. E. Youngman, *J. Phys. Chem. B*, 2004, **108**, 7557–7564.

14 K. Liao, A. Masuno, A. Taguchi, H. Moriwake, H. Inoue and T. Mizoguchi, *J. Phys. Chem. Lett.*, 2010, **11**, 9637–9642.

15 S. H. Risbud and J. A. Pask, *J. Am. Ceram. Soc.*, 1977, **60**, 418–424.

16 M. Djuric and A. Mihajlov, *J. Am. Ceram. Soc.*, 1996, **79**, 1252–1256.

17 R. Weber, S. Sen, R. E. Youngman, R. T. Hart and C. J. Benmore, *J. Phys. Chem. B*, 2008, **112**, 16726–16733.

18 P. McMillan and B. Piriou, *J. Non-Cryst. Solids*, 1982, **53**, 279–298.

19 H. Morikawa, S. Miwa, M. Miyake, F. Marumo and T. Sata, *J. Am. Ceram. Soc.*, 1982, **65**, 78–81.

20 M. Okuno, N. Zotov, M. Schmücker and H. Schneider, *J. Non-Cryst. Solids*, 2005, **351**, 1032–1038.

21 R. K. Sato, P. F. McMillan, P. Dennison and R. Dupree, *J. Phys. Chem.*, 1991, **95**, 4483–4489.

22 B. T. Poe, P. F. McMillan, C. A. Angell and R. K. Sato, *Chem. Geol.*, 1992, **96**, 333–349.

23 C. Meade and R. Jeanloz, *Phys. Rev. B*, 1987, **35**, 236–244.

24 T. Sato and N. Funamori, *Phys. Rev. B*, 2008, **101**, 255502.

25 S. Petitgirard, W. J. Malfait, B. Journaux, I. E. Collings, E. S. Jennings, I. Blanchard, I. Kantor, A. Kurnosov, M. Cotte, T. Dane, M. Burghammer and D. C. Rubie, *Phys. Rev. Lett.*, 2017, **119**, 215701.

26 Y. Kono, K. Ohara, N. M. Kondo, H. Yamada, S. Hiroi, F. Noritake, K. Nitta, O. Sekizawa, Y. Higo, Y. Tange, H. Yumoto, T. Koyama, H. Yamazaki, Y. Senba, H. Ohashi, S. Goto, I. Inoue, Y. Hayashi, K. Tamasaku, T. Osaka, J. Yamada and M. Yabashi, *Nat. Commun.*, 2022, **13**, 2292.

27 C. Meade, R. J. Hemley and H. K. Mao, *Phys. Rev. Lett.*, 1992, **69**, 1387–1390.

28 C. J. Benmore, E. Soignard, S. A. Amin, M. Guthrie, S. D. Shastri, P. L. Lee and J. L. Yarger, *Phys. Rev. B*, 2010, **81**, 054105.

29 T. Sato and N. Funamori, *Phys. Rev. B*, 2010, **82**, 184102.

30 A. Zeidler, K. Wezka, R. F. Rowlands, D. A. J. Whittaker, P. S. Salmon, A. Polidori, J. W. E. Drewitt, S. Klotz, H. E. Fischer, M. C. Wilding, C. L. Bull, M. G. Tucker and M. Wilson, *Phys. Rev. Lett.*, 2014, **113**, 135501.

31 C. Prescher, V. B. Prakapenka, J. Stefanski, S. Jahn, L. B. Skinner and Y. Wang, *Proc. Natl. Acad. Sci. U. S. A.*, 2017, **114**, 10041–10046.

32 Y. Kono, Y. Shu, C. Kenney-Benson, Y. Wang and G. Shen, *Phys. Rev. Lett.*, 2020, **125**, 205701.

33 A. Yokoyama, M. Matsui, Y. Higo, Y. Kono, T. Irifune and K.-i. Funakoshi, *J. Appl. Phys.*, 2022, **107**, 123530.

34 C.-s. Zha, R. J. Hemley, H.-k. Mao, T. S. Duffy and C. Meade, *Phys. Rev. B*, 1994, **50**, 13105–13112.

35 C. Weigel, M. Mebarki, S. Clément, R. Vacher, M. Foret and B. Rufflé, *Phys. Rev. B*, 2019, **100**, 094102.

36 I. Ohira, Y. Kono, S. Gréaux, J. W. E. Drewitt, S. Jahn, F. Noritake, K. Ohara, S. Hiroi, N. M. Kondo, R. Hrubiak, Y. Higo, N. Tsujino, S. Kakizawa, K. Nitta and O. Sekizawa, *Phys. Rev. B*, 2024, **110**, 054115.

37 Y. Kono, C. Park, C. Kenney-Benson, G. Shen and Y.Wang, *Phys. Earth Planet. Inter.*, 2014, **228**, 269–280.

38 T. Tsuchiya, *J. Geophys. Res.: Solid Earth*, 2003, **108**, 2462.

39 R. Hrubiak and M. L. Rivers, *High Press. Res.*, 2023, **43**, 175–191.

40 Y. Kono, K. Ohara, N. M. Kondo, Y. Higo, S. Kakizawa, H. Yumoto, T. Koyama, H. Yamazaki, Y. Senba, H. Ohashi, I. Inoue, Y. Hayashi and M. Yabashi, *Rev. Sci. Instrum.*, 2024, **95**, 013904.

41 Y. Higo, Y. Kono, T. Inoue, T. Irifune and K.-i. Funakoshi, *J. Synchrotron. Rad.*, 2009, **16**, 762–768.

42 Y. Higo, T. Irifune and K.-i. Funakoshi, *Rev. Sci. Instrum.*, 2018, **89**, 014501.

43 Y. Kono, C. Park, T. Sakamaki, C. Kenney-Benson, G. Shen and Y. Wang, *Rev. Sci. Instrum.*, 2012, **83**, 033905.

44 Y. Onodera, S. Kohara, P. S. Salmon, A. Hirata, N. Nishiyama, S. Kitani, A. Zeidler, M. Shiga, A. Masuno, H. Inoue, S. Tahara, A. Polidori, H. E. Fischer, T. Mori, S. Kojima, H. Kawaji, A. I. Kolesnikov, M. B. Stone, M. G. Tucker, M. T. McDonnell, A. C. Hannon, Y. Hiraoka, I. Obayashi, T. Nakamura, J. Akola, Y. Fujii, K. Ohara, T. Taniguchi and O. Sakata, *NPG Asia Mater.*, 2020, **12**, 85.

45 R. D. Shannon, *Acta. Cryst. A*, 1976, **32**, 751–767.

46 S. K. Lee, K. Y. Mun, Y.-H. Kim, J. Lhee, T. Okuchi and J.-F. Lin, *J. Phys. Chem. Lett.*, 2020, **11**, 2917–2924.

47 S. K. Lee, E. El Ghazaoui, J. J. Kweon, S. Lee and J.-H. Parq, *Nat. Commun.*, 2025, **16**, 9930.

48 T. Rouxel, *J. Am. Ceram. Soc.*, 2007, **90**, 3019–3039.

49 W. H. Wang, C. Dong and C. H. Shek, *Mater. Sci. Eng.*, 2004, **R44**, 45–89.

50 W. H. Wang, *Prog. Mater. Sci.*, 2012, **57**, 487–656.

View Article Online
DOI: 10.1039/D6MA00275G

Data Availability Statement

February 27, 2026

Dear Editor of Materials Advances,

The data supporting this article have been included as part of the supplementary information (SI). Supplementary information: Schematic diagram of the high-pressure cell for sound velocity measurement, Structure factor [$S(Q)$] and pair-distribution function [$g(r)$] with vertical offset, pressure dependence of $r1$ and sample length, and numerical values of measured sound velocity and chemical composition.

Thank you very much for your consideration.

Sincerely yours,
Itaru OHIRA, Ph.D. (Corresponding author)

Department of Chemistry, Faculty of Science, Gakushuin University
1-5-1, Mejiro, Toshima-ku, Tokyo 171-8588, Japan.
E-mail: itaru.ohira@gakushuin.ac.jp
TEL: +81-3-5904-9378